

Full length article

Segregation-enhanced grain boundary embrittlement of recrystallised tungsten evidenced by site-specific microcantilever fracture

Chunhua Tian^{a,1}, Yan Ma^a, Alireza Ghafarollahi^a, Piyush Patil^a, Gerhard Dehm^a, Erik Bitzek^a, Marcin Rasinski^b, James P. Best^{a,*}

^a Max-Planck-Institut für Eisenforschung GmbH, Max-Planck-Str. 1, D-40237 Düsseldorf, Germany

^b Forschungszentrum Jülich GmbH, Institut für Energie- und Klimaforschung, D-52425 Jülich, Germany

ARTICLE INFO

Keywords:

Microcantilever
Fracture toughness
Grain boundaries
Tungsten
Embrittlement
Segregation
Atomistic simulation
Crack – grain boundary interaction

ABSTRACT

Tungsten stands a prime candidate for plasma-facing applications in fusion reactors, attributed to its capacity to withstand high temperatures and intensive particle fluxes. The operational heat flux, however, can induce recrystallisation of the initial microstructure, increasing the brittle-to-ductile transition temperature. Although such a phenomenon is thought to result from impurity segregation to grain boundaries, direct evidence of impurity-induced grain boundary embrittlement has not yet been reported. Addressing this, our study employs microcantilever testing, coupled with local chemical analysis via atom probe tomography, to unveil the impact of impurity segregation on the fracture toughness of recrystallised tungsten with a purity of 99.98 at.%. The *in situ* fracture toughness measurements were performed with the notch placed directly at random high-angle grain boundaries, revealing brittle failure regardless of grain boundary misorientation or grain orientation. Notably, both single-crystalline microcantilevers and the as-received material exhibited significant plasticity before failure, with instances without crack propagation. In contrast, recrystallised grain boundaries displayed a fracture toughness of $4.7 \pm 0.4 \text{ MPa}\cdot\sqrt{\text{m}}$, determined using a linear elastic approach - notably lower than for cleavage plane fracture in tungsten microcantilevers. Local atom probe analysis of the high-angle grain boundaries exposed phosphorous segregation exceeding 2 at.% at the recrystallised interfaces, stemming from recrystallisation. Atomistic simulations confirmed the role of phosphorous in embrittling high-angle grain boundaries in tungsten, while additionally revealing mechanisms of crack-grain boundary interactions and their dependence on phosphorous segregation.

1. Introduction

Tungsten is considered as a key material for plasma-facing components for current (JET [1], ASDEX Upgrade [2], WEST [3]) and future (ITER [4]) fusion reactors. For such applications, tungsten benefits from its high melting point, high-temperature strength, good thermal conductivity, and high sputtering threshold under hydrogen bombardment [5,6]. In addition, the accumulation of radioactive tritium is much lower than in carbon-dominated machines [7]. The major drawback of tungsten utilisation is, however, its brittle behaviour at low operating temperatures below its brittle-to-ductile transition temperature (BDTT) of around 300–400 °C [8]. Additionally, a more brittle mechanical response has often been reported when the material is recrystallised [9,

10]. Peak operation temperatures of ~2000 °C, above the recrystallisation temperature of tungsten, followed by lower temperatures at later stages could therefore lead to brittle material failure with unstable crack propagation and a reduction of component lifetimes [11]. The recrystallisation kinetics and damage initiation for tungsten in conditions approximating fusion conditions have been recently studied [12,13]. The promoted embrittlement of recrystallised tungsten (RXW) is often reported to depend on the amount and type of impurity in even nominally high-purity tungsten [9]. Highlighting the role of kinetic impurity segregation in recrystallised tungsten, embrittlement has been shown to be avoided after pulsed high heat flux thermal treatment, although the combination of high-purity tungsten, initial coarse microstructure, and low defect density may also play a significant role [9]. Segregation of

* Corresponding author.

E-mail address: j.best@mpie.de (J.P. Best).

¹ Current address: Laboratory for Mechanics of Materials and Nanostructures, Empa – Swiss Federal Institute for Materials Science and Technology, CH-3603 Thun, Switzerland.

<https://doi.org/10.1016/j.actamat.2023.119256>

Received 12 December 2022; Received in revised form 11 August 2023; Accepted 14 August 2023

Available online 14 August 2023

1359-6454/© 2023 The Authors. Published by Elsevier Ltd on behalf of Acta Materialia Inc. This is an open access article under the CC BY-NC-ND license (<http://creativecommons.org/licenses/by-nc-nd/4.0/>).

impurities at grain boundaries (GBs) is well-known to influence GB cohesion [14]. Segregation can additionally affect dislocation-GB interactions like limiting transmission which can lead to crack nucleation and promote brittle intergranular fracture [15].

Great efforts have been made in the last decades to study the role of various impurity elements on the embrittling effects of segregated solutes at GBs through chemical investigation of bulk-scale specimen fracture surfaces [16]. More recently, first-principle calculations of the segregation energy and the work of separation on individual, symmetric low Σ GBs [17–20] confirmed that phosphorous at the GBs reduces the GB cohesion. These calculations, however, only studied phosphorous atoms at specific GB sites at low coverage, not allowing for direct P-P interactions, and did not address more general GBs. Furthermore, calculating the work of separation does not include an actual crack, and kinetic effects like lattice-trapping, which were shown to lead to significant deviations in the fracture toughness compared to the predictions by the work of separation [21,22], are not included in these approaches. There remain a number of open questions on the key elements for embrittlement and severity of the segregation on local toughness (the introduction of Ref. [9] gives a good overview). The picture from the literature is far from consistent, with contradicting results for some elements. Macroscopic studies show conflicting reports regarding the role of segregating impurity species on the mechanical response; while carbon has been considered critical [23], other studies state that phosphorous, potassium or oxygen, or combinations thereof, dictate the mechanical response [24]. Key studies in the field have shown with Auger electron spectroscopy that both phosphorous and carbon, in conjunction with nickel and iron, segregate to tungsten grain boundaries [16], obscuring a clear understanding as to the function of each impurity species. Discrepancy further arises when simulating the influence of elements on the GB cohesion, due to the dependence of GB atomic positions which are considered for the segregating species. The occupied site (e.g. interstitial or substitutional) has been shown to strongly affect both segregation energies and strength of embrittlement [14,25]. However, these studies were performed on symmetric $\Sigma 3[110](-111)$ GBs with a rather open GB structure. In view of a recent study [26] it seems questionable in how far their results on such special GBs can be generalised. Finally, there is the question how important the embrittlement of GBs by segregants in tungsten is compared to other effects. Based on an increasing proportion of transgranular fracture detected with increasing recrystallisation temperatures Gludovatz *et al.* showed that the microstructure and dislocation density within the grains can be more critical factors than the segregation of impurities in polycrystalline tungsten [23].

Due to the uncertainty surrounding the effects of impurity segregation at GBs in RXW, notched bicrystalline microcantilever testing can serve as an important technique to extract site-specific quantitative fracture toughness data as a function of geometrical and chemical GB parameters. Indeed, the fracture toughness of polycrystalline tungsten is well characterised at both macro- [27] and microscopic scales [28]. Microcantilever investigations have recently allowed for targeted investigation of single crystal response and in particular the toughness of cleavage planes as for $\langle 100 \rangle \{100\}$ in the *bcc* crystal lattice of tungsten [28–30]. Recently, microcantilever tests were performed on ultrafine-grained polycrystalline tungsten with hafnium and boron GB segregation, which was resolved to improve the bending strength and ductility by enhancing the GB cohesion [31], however no existing microcantilever study on tungsten has considered testing individual GBs. A clear advantage for such bicrystalline microcantilever beams is that the sharp notches necessary for toughness measurement can be milled directly at GBs of interest, and then used in tandem with a local chemical analysis tool, such as atom probe tomography (APT), to rationalise local chemical effects on the fracture behaviour.

To unravel the role of GB chemistry on embrittlement of RXW, site-specific microcantilever measurements are made on nominally pure as-received and recrystallised tungsten, whereby both the grain boundaries

and single-crystalline grain interiors are tested for the recrystallised material. Samples were first investigated using electron backscattered diffraction (EBSD) and cantilevers subsequently cut at either GBs or within single-crystal volumes, and *in situ* testing performed to evaluate the fracture toughness. Using the collected EBSD information, the fracture toughness could then be understood in relation to the crystallographic parameters of the studied GBs in RXW. To correlate the local chemistry of grain boundaries to the measured fracture toughness, equivalent random high-angle GBs were analysed by APT. The obtained results were finally rationalised by performing atomistic fracture simulations along both pure, and phosphorous-segregated, asymmetric $\Sigma 7$ GBs which were modelled after an experimentally-tested GB. Taken together, the obtained experimental and simulation results provide clear insights into the role of chemical segregation to GBs on the embrittlement of recrystallised tungsten.

2. Materials and methods

2.1. Sample fabrication and microstructural characterisation

The sample used in this work is nominally pure tungsten manufactured by Plansee Group. By impurity analysis as shown in Table 1, the tungsten sample has a purity higher than 99.98 at.% determined using inductively coupled plasma mass spectrometry (ICP-MS) and inductively coupled plasma optical emission spectroscopy (ICP-OES). It is noted that phosphorous, though an element of interest, cannot be quantified here since the applied liquefying solution for wet chemistry analysis already contains phosphorous. Small samples with $8 \times 8 \times 8$ mm were cut from the commercial as-received bar with dimension $40 \times 40 \times 300$ mm, produced by standard sintering and two-directional forging. The smaller sample studied in this work was then recrystallised at 1600 °C for 1 h. Before any microstructural characterisation, the top surface of the specimen (normal to the elongation direction of forged grains) was metallographically prepared. A final polish was achieved using silica OPS suspension containing H_2O_2 . Additionally, the side faces were ground to minimise the influence of roughness and contamination generated by mechanical cutting on the preparation of microcantilevers at the edge. A reference sample of the as-received material was similarly prepared for comparison. Subsequent microstructure investigation was performed using scanning electron microscopy (SEM) with Zeiss Auriga and Zeiss Gemini500 machines. EBSD measurements were conducted on the same Zeiss Auriga microscope equipped with an EDAX system and Hikari charge-coupled device (CCD) camera. The orientation information was compiled through the TSL OIM v7 software package. An applied acceleration voltage of 15 kV was used, with an aperture size of 120 μ m and step size of 300 nm.

2.2. Mechanical characterisation

Rectangular microcantilevers were milled at the sample edge using a focused ion beam (FIB, Zeiss Auriga dual-beam workstation) for the as-received microstructure and the RXW samples. The microcantilevers of the RXW samples either targeted at grain boundaries or the single grain regions, while for the much finer grained as-received material the notch was always placed in the vicinity of a grain boundary. First, a fine cross-sectional polishing cut with 240 pA Ga^+ ion current was made to confirm whether targeted grain boundary planes were sufficiently straight and orthogonal to the top surface plane. After identifying GBs for testing, microcantilevers were coarsely milled in an FEI Helios Plasma FIB. A 60 μ A Xe^+ ion current was applied to accelerate the fabrication process. The coarsely milled beams were then finely prepared again with the gallium source FIB, using 16 nA, 2 nA and 600 pA ion currents in sequence for near-net-shape beams. The final procedure was the creation of a pre-crack. In this work, bridge-free straight notches were targeted. For that, a line pattern longer than beam width (B) was milled with 50 pA on the beams. Since this step resulted in over-milled

Table 1

Impurity content measured for the investigated nominally pure as-received tungsten sample. The tungsten purity >99.994 wt.%, equivalent to >99.98 at.%.

	Al	Fe	H	Cd	Cr	K	Mo	N	Hg
($\mu\text{g/g}$)	<3	7.1	0.0001	0.01	3.18	<30	6	0.0004	<2
	Cu	Ni	C	O	Pb	Re	Ta	S	P
($\mu\text{g/g}$)	<0.7	<10	0.0012	0.0004	<0.008	<0.5	<2	<0.0013	–

pre-cracks at the beam sides as discussed in Ref. [32], the two sides of the beams were therefore finally polished using 600 pA to minimise the over-milled segments on the pre-cracks. However, through this milling process, some curtaining artefacts were also observed to occur localised at the notch. In all cases the acceleration voltage was 30 kV.

All *in situ* microcantilever bending tests were performed in a Zeiss Gemini500 equipped with an ASMEC Unat II device (Asmec GmbH, Germany) in displacement-controlled mode. A conical diamond indenter tip was used for testing (Synton MDP AG, Switzerland) with a loading rate of 10 nm/s. The beams underwent continuous loading/unloading cycles with increasing total displacement until either fracture occurred or a displacement of 5 μm was reached. The loading/unloading sequences allowed for the determination of the stiffness change during the test for obtaining the related crack extension. The generated force-displacement data was processed by programming scripts in Wolfram Mathematica, combined with the previously measured geometrical dimensions. Depending on whether the tested beams exhibit brittle fracture or not, either linear elastic fracture mechanics (LEFM) or elastic-plastic fracture mechanics (EPFM) was applied for the evaluation of fracture toughness.

For LEFM analysis, the stress intensity factor K_I describing the stress distribution in the singularity-dominated zone can be calculated through Eq. (1):

$$K_{IQ} = \frac{F_Q L}{BW^{\frac{3}{2}}} f\left(\frac{a}{W}\right) \quad (1)$$

Note that subscript Q is used as the conditional K_I obtained through microcantilever testing is not reflective of the geometry-independent material property. L , B , W and a are beam dimensions, representing the length from the notch line to the loading point, width, height and notch depth, respectively. F_Q is the critical load, captured through a 5% secant line (line starting from the origin with a slope equal to 95% of the initial elastic loading slope) per ASTM E399 [33]. Due to minor noise in the load signal, force-displacement data was first fitted with a high-order polynomial smoothing function to determine a unique force value (the intersection of 5% secant line and the polynomial). The term $f\left(\frac{a}{W}\right)$ denotes the geometry function corresponding to a specific beam type. For single cantilever beams in this work, $f\left(\frac{a}{W}\right)$ is formulated as Eq. (2) [34]:

$$f\left(\frac{a}{W}\right) = 1.46 + 24.36\left(\frac{a}{W}\right) - 47.21\left(\frac{a}{W}\right)^2 + 75.18\left(\frac{a}{W}\right)^3 \quad (2)$$

For EPFM analysis, the J integral is calculated to assess fracture toughness, taking both the elastic energy and dissipated plastic energy into account:

$$J_{(i)} = \frac{(K_{IQ(i)})^2(1-\nu^2)}{E} + \frac{\eta A_{pl(i)}}{B(W-a_0)} \quad (3)$$

In the elastic contribution part, $K_{IQ(i)}$ is similarly determined with Eq. (1). The subscript i represents the i^{th} loading/unloading cycle. η is a dimensionless constant, as an approximation, equal to 2 for convenience in this beam geometry. E is the elastic modulus and ν the Poisson's ratio. $A_{pl(i)}$ is the plastic area component under the force-displacement curve integrated until the i^{th} unloading starting point (excluding the elastic energy area). Finally, a series of $J_{(i)}$ integral values are obtained corresponding to each unloading sequence. To achieve the final J - R curve, EPFM still requires crack extension at each unloading sequence to obtain $\{J_{(i)}, \Delta a_{(i)}\}$ pairs. The crack length $a_{(i)}$ upon each loading/unloading

cycle can be correlated with the unloading stiffness $k_{(i)}$ by fitting a straight line over each unloading segment:

$$a_{(i)} = W - \sqrt[3]{\frac{4k_{(i)}L^3}{BE}} \quad (4)$$

Hence, the crack extension $\Delta a_{(i)}$ simply equals $a_{(i)}$ subtracted by initial crack length a_0 . The $\{J_{(i)}, \Delta a_{(i)}\}$ were subsequently fit with a power-law expression:

$$J_{(i)} = C_1 (\Delta a_{(i)})^{C_2} \quad (5)$$

From the fitted J - R curve, the fracture initiation toughness J_{IQ} is determined by the criterion established in Ref. [35], from the intersection of a vertical line with the J - R curve at $\Delta a = 0.02W$, as the regulated 0.2 mm offset line with a slope of $2\sigma_y$ (yield strength) in ASTM 1820 [36] for macroscale samples is not possible for the microscale fracture tests.

2.3. Atom probe tomography

To aid the interpretation of the obtained mechanical data, APT measurements were performed on the samples containing grain boundaries for both as-received and RXW conditions. Wedges containing a grain boundary were lifted out using an FEI Helios NanoLab 600TM with 9.3 nA Ga^+ ion current, and needle-like sharp tips were consecutively milled step-by-step with 0.23 nA, 80 pA and 24 pA probe currents. An acceleration voltage of 30 kV was used. Finally, the tips with approximate 80–90 nm diameter were cleaned with a 5 kV beam and a current of 15 pA to minimise the contamination of Ga ions. The sharpened tips were evaporated atom by atom on a CAMECA instrument LEAPTM 5000XR using the laser mode. The operation parameters were set as follows: the base temperature was 55–60 K, the detection rate per laser pulse 0.5%, the laser pulse energy 70–125 pJ and the pulse rate 100–200 kHz. The reconstruction of a three-dimensional tip was performed using the software package AP Suite 6.1.

2.4. Atomistic simulations of grain boundary fracture

All simulations were performed using LAMMPS [37]. The interatomic interactions were modelled through a MEAM potential which was specifically fit to study GB fracture in W with P segregation [20,22]. Tungsten is largely an ideal model material as due to its elastic isotropy, the crack tip stress field remains well-defined, also in the presence of a GB.

To assess the effects of the segregation of phosphorous to tungsten GBs, the B7 GB from experiments was used (see Table 2) as an exemplary GB. Using the approach detailed in [38] to determine the symmetry-related variants for a given misorientation, this GB could be approximated by a $\Sigma 7$ [111] 38.21° GB that has an orientation distance of 1.6° from the experimental one. The experimental GB plane $(316 - 44 - 130)_A \parallel (82 - 69 - 25)_B$ was approximated by $(8 - 3 - 5)_A \parallel (1 - 1 - 0)_B$, with the subscripts A and B denoting the two grains joined by the GB. This GB was realised in a simulation box in which the grains have the orientations A: $x \parallel [2 \bar{1} 3 \ 11]$, $y \parallel [8 \bar{3} \ 5]$, $z \parallel [1 \ 1 \ 1]$ and Grain B: $x \parallel [\bar{1} \ \bar{1} \ 2]$, $y \parallel [1 \ \bar{1} \ 0]$, $z \parallel [1 \ 1 \ 1]$, where x and z are along the GB plane and y is the GB normal plane, as shown in Fig. S1 in the Supplementary Information. The simulation cell has dimensions of approx. 50 nm \times 60 nm \times 1 nm containing approx. 2.8×10^5 atoms.

To find the ground state structure of the GB we follow Ref. [39]. The microscopic degrees of freedom of the GB were explored by displacing the crystals relative to each other along x and z and by deleting atoms closer than $r = 0.135$ nm. Each configuration was then minimised using the conjugate gradient method while allowing displacements only along the y -direction. Once the lowest energy configuration is found this way, it is fully relaxed allowing all atoms to move. The resulting minimum energy configuration is shown in Fig. S2 in the Supplementary Information.

To mimic the diffusion during the heat-treatment of the recrystallisation process, we performed MD/MC simulations in the canonical ensemble at 600 K. This temperature was chosen so that the cooling down from 1307 K could be captured. The minimised sample was homogeneously expanded to match the thermal expansion of W and the upper and lowermost atoms in y -direction were fixed in 1.2 nm thick layers. The sample was then equilibrated for 0.2 ns using a Nose-Hoover thermostat. Using initially randomly distributed substitutional P according to the concentrations of approx. 2.5 at.% found at the recrystallised GBs, 100 MC swaps were conducted at every 1000 NVT MD steps without conservation of kinetic energy after atom swaps, following the methodology in Ref. [40]. After 5 ns of MD/MC (with a time step of 0.001 ps) the potential energy remained constant, indicating that thermal equilibrium was reached. The sample was then minimised using FIRE [41]. The equilibration by MD together with the final minimisation should ensure that the P atoms find their optimal, minimum-energy positions.

To study fracture, atoms at the y -boundaries are fixed, while the atoms at the x -boundaries were restricted to move only in y and z -directions. An edge crack was introduced together with an applied uniaxial strain field ϵ_{yy} following [42] (see Fig. S1). The homogeneous strain field in front of the crack provides a constant crack driving force

G . Several crack positions (directly on the GB and at different distances from the GB) and two crack propagation directions were tested, as the GB breaks the symmetry of the sample. The setup with the labels used later in the tables is shown in Fig. S1. For each crack tip position, we use energy minimisation to determine the initial strain ϵ_{in} at which the crack remains stable and below which crack closure occurs. Subsequently, we incrementally increase the applied strain and relax the sample in a quasi-static fashion using increments of $\Delta\epsilon = 0.001$ until the crack propagates, corresponding to the critical strain ϵ_{cr_ini} . Depending on the local situation, the crack might not propagate through the entire sample. Therefore, the strain at which the sample is separated in two is called ϵ_{cr_fi} . Defect analysis was performed using the common neighbour analysis (CNA) [43]. All analysis and visualisation were performed with Ovito [44]. Additional simulations in a K -controlled setup were performed in for a single crystal with a crack orientation taken from a representative sample in Fig. 3. For more details see the Methods section in the Supplementary Information.

3. Results

The microstructure of both as-received and recrystallised tungsten was investigated using SEM and EBSD (Fig. 1). An average grain size of (3.4 ± 2.5) μm was determined for the as-received sample and (19 ± 7) μm for recrystallised grains separated predominately by random high-angle grain boundaries (rHAGBs). The grain size is determined based on the EBSD data from Figs. S3(c), 1(d) (misorientation angle $>2^\circ$ considered as a grain), as it better detects smaller grains that are not detectable with secondary electron imaging (as for Fig. 1(c)). Indicated by arrows in Fig. 1(c), faint GB lines are present in the putative large grains. The as-received material contains $\sim 30\%$ HAGBs (defined by a misorientation angle $>15^\circ$), $\sim 70\%$ low-angle GBs (LAGBs), and is

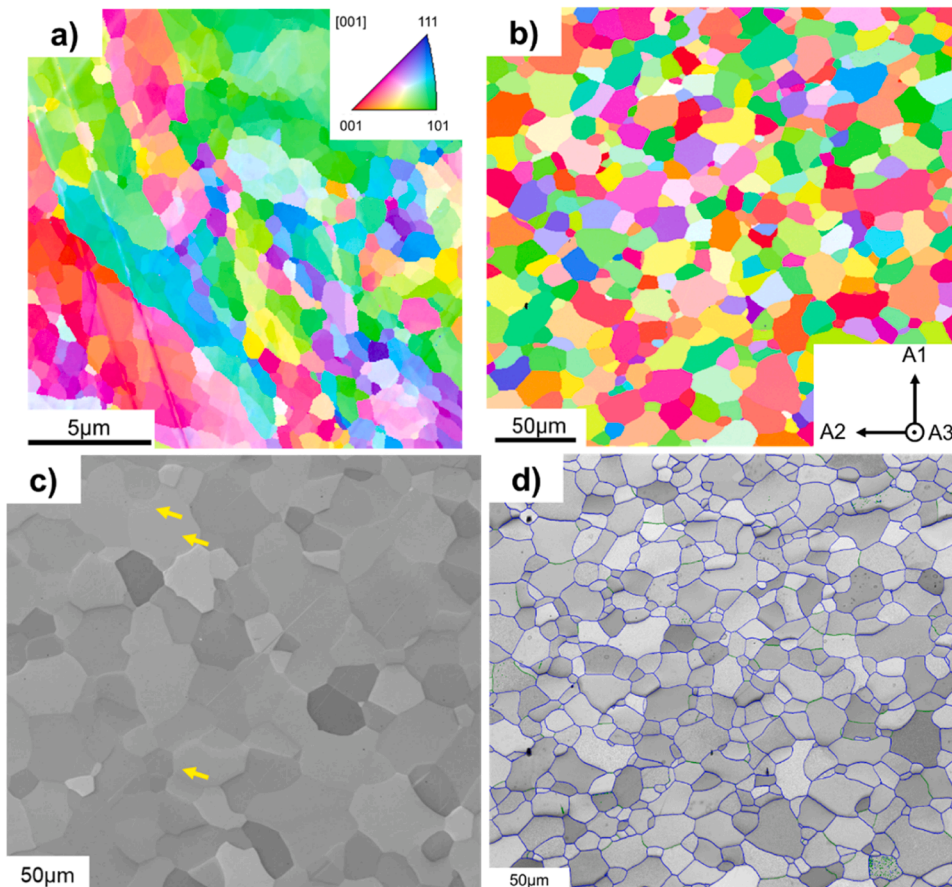


Fig. 1. Microstructure of as-received (AR) and recrystallised (RX) tungsten samples. EBSD IPF maps for as-received (a) and recrystallised (b) tungsten. The inset in (b) shows the sample reference frame. (c) SEM image under secondary electron mode of RX sample. (d) Image quality map of RX sample overlaid with grain boundary (GB) type probed by EBSD. Green represents low-angle GBs with a misorientation angle smaller than 15° ; Blue outlines the high-angle GBs ($>15^\circ$). The arrows in (c) highlight faint GBs in the putative large grains. (For interpretation of the references to colour in this figure legend, the reader is referred to the web version of this article.)

textured with a high intensity around $\{110\}$ on the $[001]$ inverse pole figure (IPF) texture plot, as shown in Fig. S3e. For the RXW the rHAGBs are highlighted as blue lines on the image quality map in Fig. 1(d), the fraction of which is much higher than LAGBs (green). Numerically, HAGBs account for $\sim 92\%$ of the total boundary length in Fig. 1(d) (including $\sim 19\%$ CSL) and LAGBs 8%. The recrystallised tungsten is highly textured with high intensity of $\{100\}$ and $\{110\}$ on an $[001]$ IPF texture plot as presented in Fig. S3f (Supplementary Information).

3.1. Microcantilever fracture tests of as-received tungsten

To serve as a baseline for interpreting the fracture results of the recrystallised tungsten grain boundaries, notched rectangular microcantilevers were first milled into the as-received tungsten material. The specimens were prepared at the edge of the sample, with a target geometry of $12\ \mu\text{m} \times 2.5\ \mu\text{m} \times 2.5\ \mu\text{m}$ ($L \times W \times B$). While it was attempted to place the notch directly at GBs, due to the finer grain size in comparison to RXW it was however not possible to have a single straight GB section under the notch (Fig. 2). Two notched microcantilever beams were successfully tested with alignment of the notch at the GB observable at the surface (Fig. 2(a)). Significant crack-tip plasticity and no catastrophic fracture along the GB was observed (Fig. 2(b) and (c)), with the crack propagating in an elastic-plastic manner. The gradually reducing unloading stiffness observed from the force-displacement curve is indicative of crack growth and signifies an elastic-plastic fracture behaviour (Fig. 2(b)). Using a J -integral analysis based on the results of Fig. 2(d), a conditional fracture toughness of approximately $19\ \text{MPa}\cdot\sqrt{\text{m}}$ was determined, which corresponds closely to the fracture toughness reported for misaligned notch-cleavage planes in tungsten single crystals [30], but is significantly higher than the $\sim 6\ \text{MPa}\cdot\sqrt{\text{m}}$ reported for ultrafine grained tungsten polycrystals determined using a J -integral analysis with average grain size of $790\ \text{nm}$ [28]. These results

demonstrate that for as-received W the GBs are not weak points for intergranular fracture.

3.2. Single crystal microcantilever fracture of RXW

The fracture response of RXW single crystal regions was analysed on notched microcantilevers with a rectangular cross-section. The specimens were prepared at the edge of the sample within single grains, with a targeted geometry of $12\ \mu\text{m} \times 2.5\ \mu\text{m} \times 2.5\ \mu\text{m}$ ($L \times W \times B$). Beams were tested with a random orientation of the notch plane with respect to the crystal structure. Testing was performed using a conical diamond counterbody, and a ductile response was observed, as shown in Fig. 3 with gradual reducing unloading stiffness from the load-displacement data. As shown in the higher magnification micrographs in Fig. 3(c), crack extension from the notch root was observed after significant displacement of the beam. Via EPFM analysis of the force-displacement data, the J -integral could be determined against crack extension (Fig. 3(d)). Using the criterion of critical crack extension at $0.02W$, the fracture toughness J_{IQ} could be determined. From testing of the single crystal grains, a conditional fracture toughness of $(14.5 \pm 1.3)\ \text{MPa}\cdot\sqrt{\text{m}}$ was calculated from a total of 4 cantilevers which showed crack growth (the toughness value is given as the mean plus standard error of the mean). This value is comparable to single crystal EPFM toughness results for tungsten when considering the random alignment of the notch with respect to the cleavage planes and expected misorientation ($12.5\ \text{MPa}\cdot\sqrt{\text{m}}$ if well-aligned with the $\{100\}$ cleavage plane and $15.5\ \text{MPa}\cdot\sqrt{\text{m}}$ if 25° twisted along the crack front) [30]. The influence of cleavage plane alignment on fracture behaviour can be also observed through post-deformation images with orientation information based on the $\{100\}$ pole figures (Fig. 3(e), (f)). Only 4 out of 11 randomly-oriented single-crystal beams show a load drop and stiffness decrease with crack evolution, as in Fig. 3(e) where the notch plane is

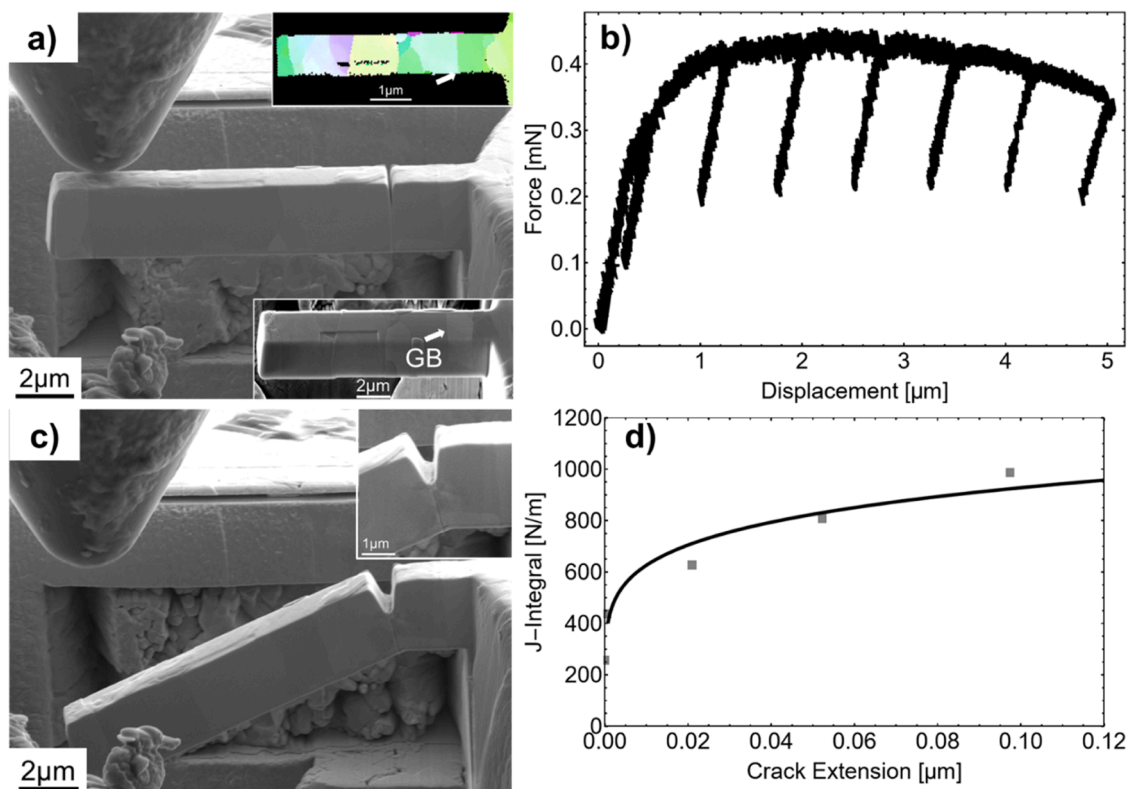


Fig. 2. Representative results of microcantilever bending tests on the as-received W sample. (a) Prepared microcantilever with notch placed at GB highlighted by white arrow (inset SEM and EBSD images). (b) Force-displacement curve tested to $5\ \mu\text{m}$. (c) Post mortem SEM micrograph showing significant crack-tip plasticity and no brittle fracture after test. (d) J -integral for the tested beam. (For interpretation of the references to colour in this figure legend, the reader is referred to the web version of this article.)

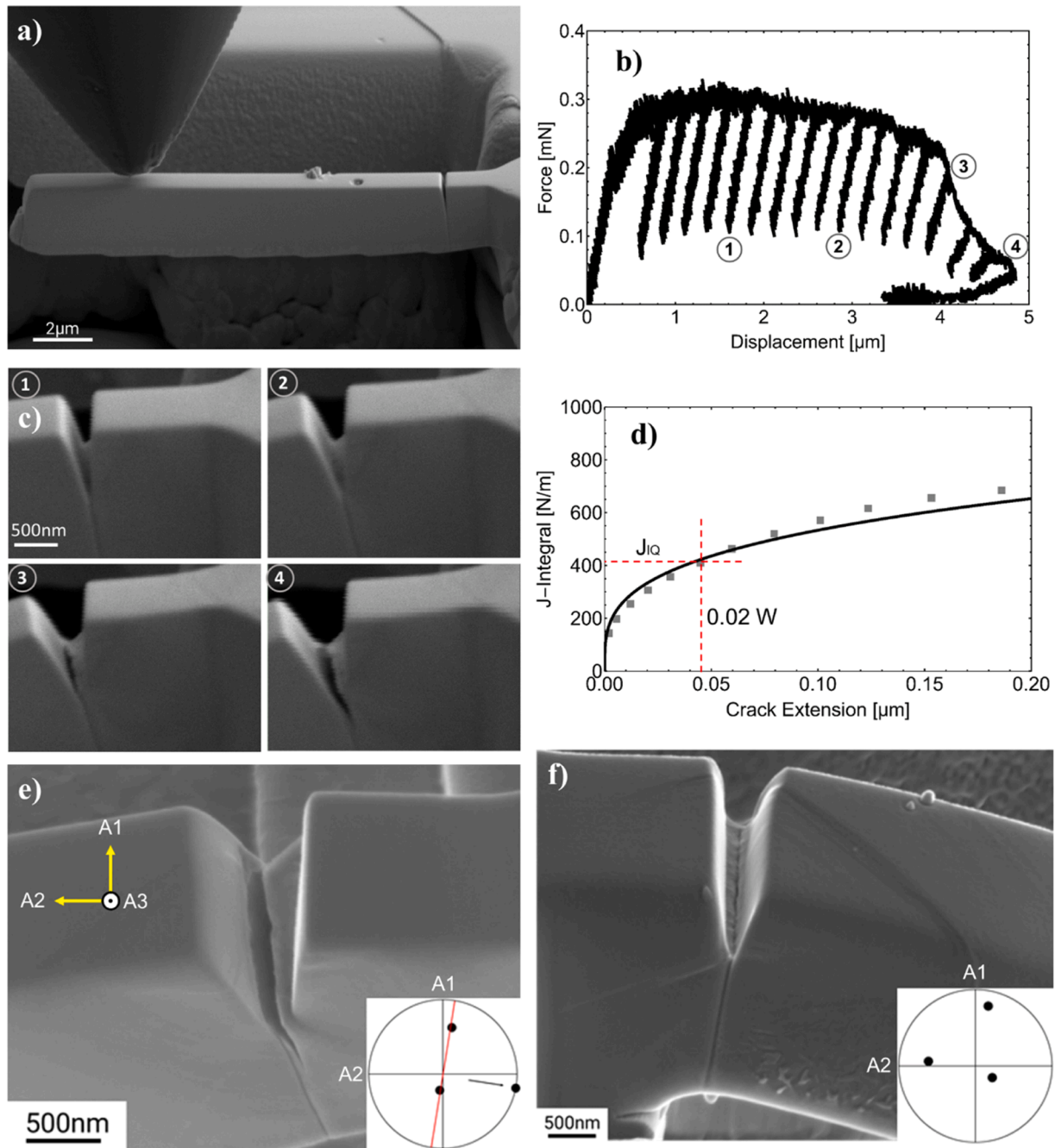


Fig. 3. Representative microcantilever fracture test of single crystal microcantilevers. (a) In situ SEM image prior to testing, while (b) the corresponding force-displacement curve implies extensive plastic deformation with continuous crack growth. (c) Snapshots from in situ recording correspond to the unloading sequence labelled in (b). (d) Extracted J -integral curve for J_{IQ} identification at $\Delta a = 0.02W$; (e) *Post-mortem* image of this tested beam with a grown crack, while (f) representative *post mortem* image is additionally shown of a single crystal beam showing no crack growth. The insets in (e) and (f) are the $\{100\}$ pole figures corresponding to these two microbeams. The red line represents the plane trace (top surface) of the pole on the great circle. (For interpretation of the references to colour in this figure legend, the reader is referred to the web version of this article.)

roughly aligned with one $\{100\}$ crack plane, while most exhibit only plastic deformation around the notch, as shown in Fig. 3(f). The crack evolution of microcantilevers fabricated in the grain interior, *i.e.* single crystalline beams, has a clear dependence on the crystallographic orientation.

3.3. Microcantilever testing at RXW grain boundaries

To test the toughness of the HAGBs ubiquitous to the RXW microstructure, microcantilevers with a rectangular cross-section cut at the

edge of the sample were again tested. GBs were targeted where the notch could be aligned parallel to the boundary. To achieve this, Ga^+ -FIB fine milling of small trenches allowed for the first confirmation of straight GB segments on both top and side surfaces (Fig. 4(a) – where a slightly misaligned GB segment in the depth is depicted). A schematic of this approach is shown in Fig. 4(b), where microcantilevers were milled at locations where straight GB segments were isolated. As highlighted in the schematic below (Fig. 4(c)), cantilevers, where the notch was placed directly at the grain boundary, contained two distinct grain orientations (represented by G1 and G2 in the schematic).

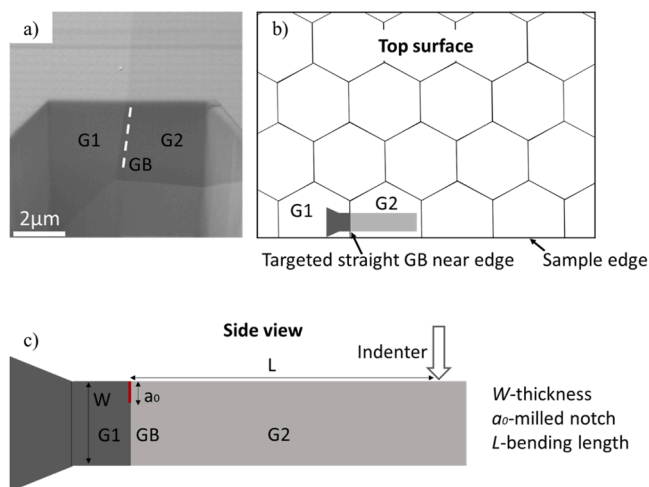


Fig. 4. (a) SE micrograph showing a FIB cross-section of a slightly angled grain boundary in the thickness direction; (b) Schematic top view of material microstructure highlighting FIB milling approach of microcantilevers targeted at straight GB segments; (c) A schematic side view of a finished beam with grain boundary, where geometric parameters are labelled.

Testing of microcantilevers with a notch aligned with the GB led to a significantly different mechanical response when compared with single-crystal RXW cantilevers. In this section, only cantilevers with accurate notch placement are considered, indicating that first the GB is well selected as a vertical plane on the beam, and secondly, with the assistance of SEM and FIB imaging, the sharp notch is placed with high accuracy at GBs on the top surface using FIB. Fig. 5(a) shows a representative micrograph of a well-aligned beam, together with an -IPF map (inset) showing different orientations of both grain pairs. In this case, during testing the mechanical response showed a more brittle failure (Fig. 5(b)), in comparison to the ductile stable crack growth shown in Fig. 3(b), signalling a significant reduction of plastic deformation under the notch root before failure. All eight cantilevers tested at the grain boundary with good placement failed in such a catastrophic manner. Cantilevers were again selected with random orientations. Based on the brittle fracture evidenced for these cantilevers, LEFM could be utilised, and an average toughness of (4.7 ± 0.4) MPa $\cdot\sqrt{m}$ was determined; significantly lower than that determined for the single

crystal beams (14.5 ± 1.3) MPa $\cdot\sqrt{m}$ and the as-received material at the GB (~ 19 MPa $\cdot\sqrt{m}$). The fracture surface of the beams with well-placed GB (inset of Fig. 5(b)) is observed to be predominantly smooth and homogeneous, typical of a brittle fracture in tungsten with no observable river-lines. However, the force-displacement curve shows some evidence of plasticity before fracture, resulting from two aspects. Firstly, the notch fabricated by FIB is not atomically sharp, and needs to gradually align itself with the exact position of GB. Second, a small segment of the GB on this specific beam is not straight along the notch plane, as indicated by the red arrow (Fig. 5(b)), where the growing crack needs to align itself along. Both alignments require extra plastic energy before brittle fracture.

3.4. RXW microcantilevers with notch plane offset to GB plane

In contrast to the well-aligned notches, the notches in a subset of 12 cantilevers were not perfectly aligned. Some GBs have a small inclination from the vertical plane, i.e., the notch normal corresponds to the cantilever beam normal, but not to the GB normal (*misaligned notches*). Other notches were not directly placed on the intersection of the GB plane with the surface, but next to the GB (*misplaced notches*). The encountered configurations are schematically shown in Fig. 6(a). An example of testing such a misaligned specimen is shown in Fig. 6, where an observable GB inclination angle (roughly 7°) from the vertical plane was determined. In this test, the mechanical force-displacement response (Fig. 6(c)) was largely comparable to that of the single crystal response in Fig. 3(b) till ~ 3 μm displacement. In contrast to the single crystal test, however, the cantilever finally fractured in a catastrophic manner along the adjacent grain boundary, as evidenced by crack evolution snapshots during testing (Fig. 6(d)). In this case, the *J-R* integral curve was constructed to extract the fracture initiation toughness of the beam with misaligned notch plane with respect to GB plane (Fig. 6(e)). In Fig. 6(e), the less accurate fitting curve is due to the fewer accumulated loading/unloading cycles limited by the catastrophic fracture before reaching the targeted displacement. The result of these tests gives an average fracture toughness of (14.0 ± 0.6) MPa $\cdot\sqrt{m}$, which is comparable to (14.5 ± 1.3) MPa $\cdot\sqrt{m}$ of the single crystals tested. Note that the average fracture toughness here of misaligned/misplaced GBs considers only the elasto-plastically fractured beams. There were additionally two beams, though with an inclined GB, which fractured in a brittle manner with K_{IQ} equivalent to 5.1 MPa $\cdot\sqrt{m}$ and 6.3 MPa $\cdot\sqrt{m}$; a comparable fracture toughness to that of the well-aligned GBs.

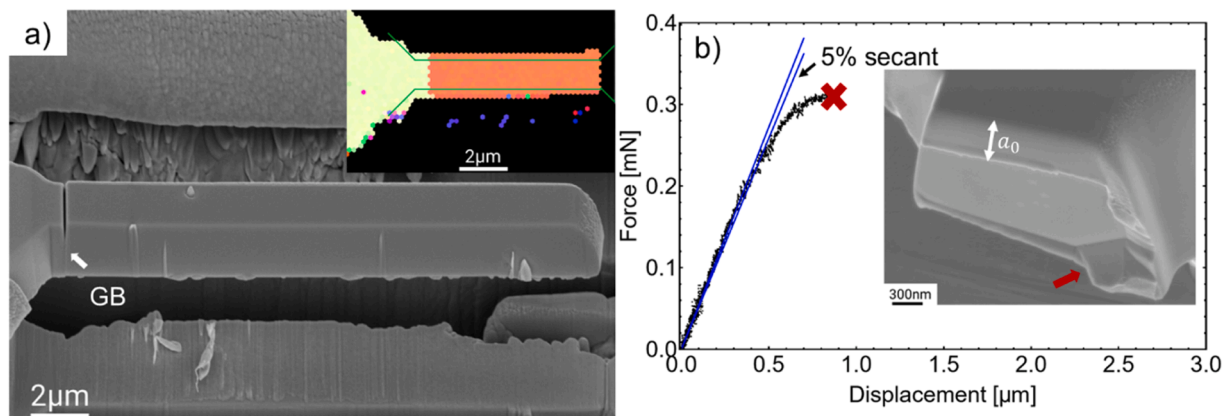


Fig. 5. (a) Microcantilever with straight GB as indicated from the EBSD IPF image (inset). The side wall from the SEM image does not show clear grain boundary contrast due to FIB milling artefacts. Note that the EBSD inset image was taken before the notch milling and final shaping (final polishing patterns shown by the green lines). A random HAGB was tested, characterised by a misorientation angle of 42.3° around the $[3,4,4]$ axis. The $(82\ 69\ 25)$ plane of the left grain and $(316\ 44\ 130)$ of the right grain align with the GB plane assuming perfect vertical continuation of the GB, confirmed for this cantilever by cross-sectional FIB imaging. (b) The corresponding force-displacement curve, characteristic of brittle fracture, is shown together with a *post-mortem* SEM image (inset). The maximum load to calculate fracture toughness K_{IQ} is obtained according to ASTM E399 using a 5% secant offset. (For interpretation of the references to colour in this figure legend, the reader is referred to the web version of this article.)

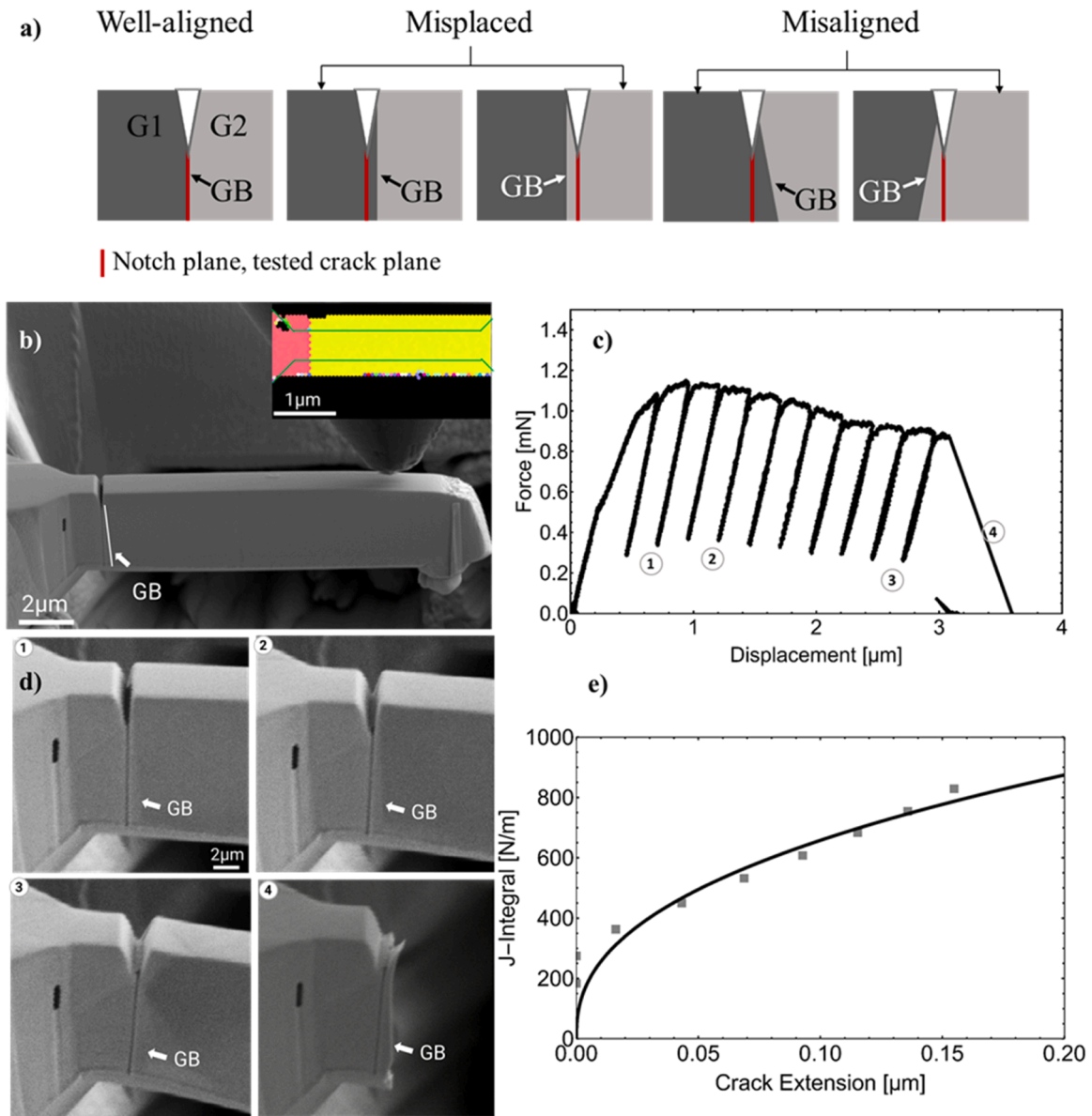


Fig. 6. (a) Side [010] view of the cantilever at the notch showing the definition of misalignment and misplacement used here. (b) A beam with grain boundary misaligned from the notch plane, as highlighted by the white arrow. From the IPF map of the top surface, the boundary is straight (inset, final polishing patterns shown by the green lines). Note that the EBSD was taken before the notch milling and final shaping. (c) The corresponding force-displacement curve implies intensive plastic deformation before a final fracture along the grain boundary, consistent with the crack evolution shown in (d), the snapshots from *in situ* recording, corresponding to unloading sequence labelled in (c). (e) Extracted *J*-integral curve. (For interpretation of the references to colour in this figure legend, the reader is referred to the web version of this article.)

The placement and alignment of the notch strongly determine if the crack can evolve in a brittle fashion along the GB. However, a GB close to the notch, either in a misplaced or misaligned situation, can provide a preferential location for crack nucleation, growth and brittle failure in the RXW samples along the GB. Importantly, 12 out of 13 RXW beams containing a misaligned/misplaced GB show crack propagation, whilst only for 4 out of 11 beams without a GB (single crystalline) exhibited crack growth. These results for misaligned and misplaced beams also demonstrate that the observed embrittlement effect is unlikely caused by ion implantation at the notch root, as brittle failure along the GB occurs adjacent to the notch plane in a volume of material which should remain pristine, *i.e.* unexposed to gallium implantation and knock-on damage.

To assist in assigning the tested notch plane, the concept of tilt and twist angle is introduced. For the tested notch plane, the notch plane

normal is symbolled as \overline{Nn} , the notch front direction is \overline{Fn} , and the third direction is $\overline{Rn} = \overline{Fn} \times \overline{Nn}$. For a single crystal, the normal of the cleavage planes is \overline{Nc} . The tilt and twist angles are defined according to Eqs. (6) and (7), respectively,

$$\theta_{tilt} = \cos^{-1}(\overline{Fn} \times \overline{Nn}) \cdot (\overline{Fn} \times \overline{Nc}) \quad (6)$$

$$\theta_{twist} = \cos^{-1}(\overline{Fn}) \cdot (\overline{Nc} \times \overline{Rn}) \quad (7)$$

In case of beams with GBs, we only consider the tilt angle between the notch plane and GB plane (e.g., the two planes rotated along the crack front direction \overline{Fn} , the case of misaligned in Fig. 6(a)), as when milling the notch, the notch line is always intended to align with the top view GB trace. For a detailed overview of the tested microcantilevers, including their geometric dimensions, the tilt angle/twist angle and the corresponding fracture toughness are summarised in Table 2. Here only

Table 2

Summary of tested microcantilever beams with geometrical dimensions, the tilt angle/twist angle and the corresponding fracture toughness. Tilt and twist angle pairs are based on the cleavage plane that gives the minimum tilt angle. Cleavage planes of {110} are considered in this table. The angles with respect to {100} are provided in Table S1.

Beams	a_0	W	B	L	a_0/W	Tilt angle	Twist angle	K_{IQ}
<i>Aligned GBs for as-received sample</i>								
B1	0.90	2.50	2.10	10.22	0.36	–	–	18.9
B2	0.90	3.2	1.40	12.05	0.28	–	–	19.4
<i>Grain Interior</i>								
B1_R	0.47	2.31	1.51	10.82	0.20	19.2°	30.9°	13.5
B2_R	0.32	2.05	3.13	12.20	0.15	6.4°	46.8°	13.6
B9_L2	0.24	1.50	2.80	11.85	0.16	0°	35.1°	12.6
B10_R1	1.13	2.70	1.84	14.23	0.42	10.4°	38.9°	18.3
<i>Aligned GBs</i>								
B7	0.70	1.93	1.97	14.00	0.36	–	–	4.6
B9_1	0.56	1.61	2.24	12.16	0.35	–	–	5.0
B9_2	0.94	3.58	1.71	12.81	0.26	–	–	5.5
B10_1	1.07	2.52	2.53	14.41	0.42	–	–	4.1
B10_2	1.35	5.28	1.84	14.65	0.26	–	–	3.9
B12_1	0.65	3.85	1.65	11.80	0.17	–	–	5.1
B12_2	1.79	5.81	1.99	10.98	0.31	–	–	6.5
B14	0.88	3.32	2.45	10.48	0.27	–	–	2.5
<i>Misaligned/misplaced GBs</i>								
B1	0.55	2.94	2.67	10.63	0.19	6.8°	–	15.2
B2	0.73	2.23	1.86	12.41	0.33	16.3°	–	13.9
B4	0.46	2.52	2.34	12.11	0.25	13.4°	–	9.7
B5	0.49	2.93	2.30	11.65	0.17	9.2°	–	15.6
B6	0.74	2.00	2.92	11.64	0.37	11.7°	–	15.7
B8	0.52	2.74	2.61	11.87	0.19	11.7°	–	13.5
B11_1	0.55	3.74	3.00	14.00	0.15	<i>misplaced/19.7°</i>	–	15.2
B11_2	1.19	6.67	1.91	13.47	0.19	19.7°	–	6.3
B13	0.51	2.22	2.77	13.46	0.23	12°	–	5.1
B16	0.64	1.90	3.26	10.57	0.34	<i>misplaced</i>	–	11.8
B17	0.70	3.60	2.02	13.15	0.19	6.4°	–	13
B18	0.81	2.42	3.04	11.19	0.33	<i>misplaced</i>	–	16.1

Notes: Units of all geometric parameters are μm while K_{IQ} is $\text{MPa}\cdot\text{m}^{1/2}$. *Misplaced* indicates that the notch line at the beam top surface is not placed correctly at the GB line, despite selection of an appropriate GB. The lateral offset is measured as 300 nm, 150 nm and 100 nm for the three *misplaced* cases B11_1, B16 and B18, respectively.

the tested beams are shown where crack growth was observed and a toughness value could be extracted.

As seen from Table 2, due to the polycrystalline nature of the sample, the tested beams in general have a wide range of out-of-plane and in-plane crystallographic orientations. Further, the alignment between the crack plane and the cleavage plane is known to influence the fracture behaviour of tungsten [30]. To check the crystallographic orientation dependence on the fracture toughness, the tested crack planes (assumed to be notch plane in this work) are shown in the [010] IPFs with the colour scale representing the magnitude of the obtained K_{IQ} values (Fig. 7(a)–(c)). Unfilled points represent tested beams without crack growth while the overlapped circles represent two beams tested at the same orientation. In the group of misaligned/misplaced GBs, the crack plane is only illustrated in the grain containing the notch (see Fig. 6(a)), while in the group of well-placed notches, GBs orientation values are provided for grains on either side of the notch plane. Grain pairs are indicated using a dotted line to connect the two orientation points. It is therefore evident that GB-containing cantilevers, even when the notch plane is misaligned or misplaced to the GB plane, are more prone to crack propagation compared with the single-crystalline grain interior (*i. e.* the fraction of unfilled points in Fig. 7(a)–(c)). Since the tested orientations are chosen randomly, the higher tendency for crack growth is therefore caused by the presence of a HAGB plane in the vicinity of a notch plane.

For single crystals, with weak tendency it appears that when the notch plane is close to {100} cleavage planes, the barrier to fracture is lower (green points near [001] in Fig. 7(a), however, the toughness is also low when aligned with {111}). A similar observation holds for well-

aligned GBs, where a {100} cleavage plane of one grain overlaps with the GB plane and has a much lower toughness so that if the GB is aligned with the cleavage plane of either grain the GB appears to be particularly brittle (Fig. 7(b)). To have a more direct visualisation of the relative misorientation between notch plane and cleavage or GB planes, for the single crystals, the K_{IQ} values are plot against the tilt and twist angle between the notch plane and {110} cleavage planes while for misaligned/misplaced GBs, against the tilt angle between notch plane and GB plane. The results are shown in Fig. 7(d), (e). The fracture toughness for the misaligned/misplaced GBs is between the values for single crystal grain interior, and well-aligned cantilever beams; highlighting the embrittling effect of the adjacent HAGB close to the notch. Based on the data set, it can be concluded that for the RXW GBs are significantly more prone to fracture with an approximately 3 times reduced K_{IQ} compared with the single crystal measurements, and 4 times reduced compared to testing the as-received GBs. No other relations such as tilt or twist angles could consistently explain the data based on the GBs tested in this work. K_{IQ} plot against the grain-pair misorientation angle is additionally presented in Fig. S4, where the toughness shows no relationship to the GB misorientation angle (data in supplementary Table S1). However, while grain crystallography is insensitive to the toughness, it is not clear if the low K_{IQ} values obtained for the “well-aligned” beams are caused by segregation-induced embrittlement at the grain boundary.

3.5. Atom probe tomography analysis of GBs in RXW

Since the GB brittleness in the recrystallised tungsten cannot be rationalised using crystallographic measures, chemical analysis by APT

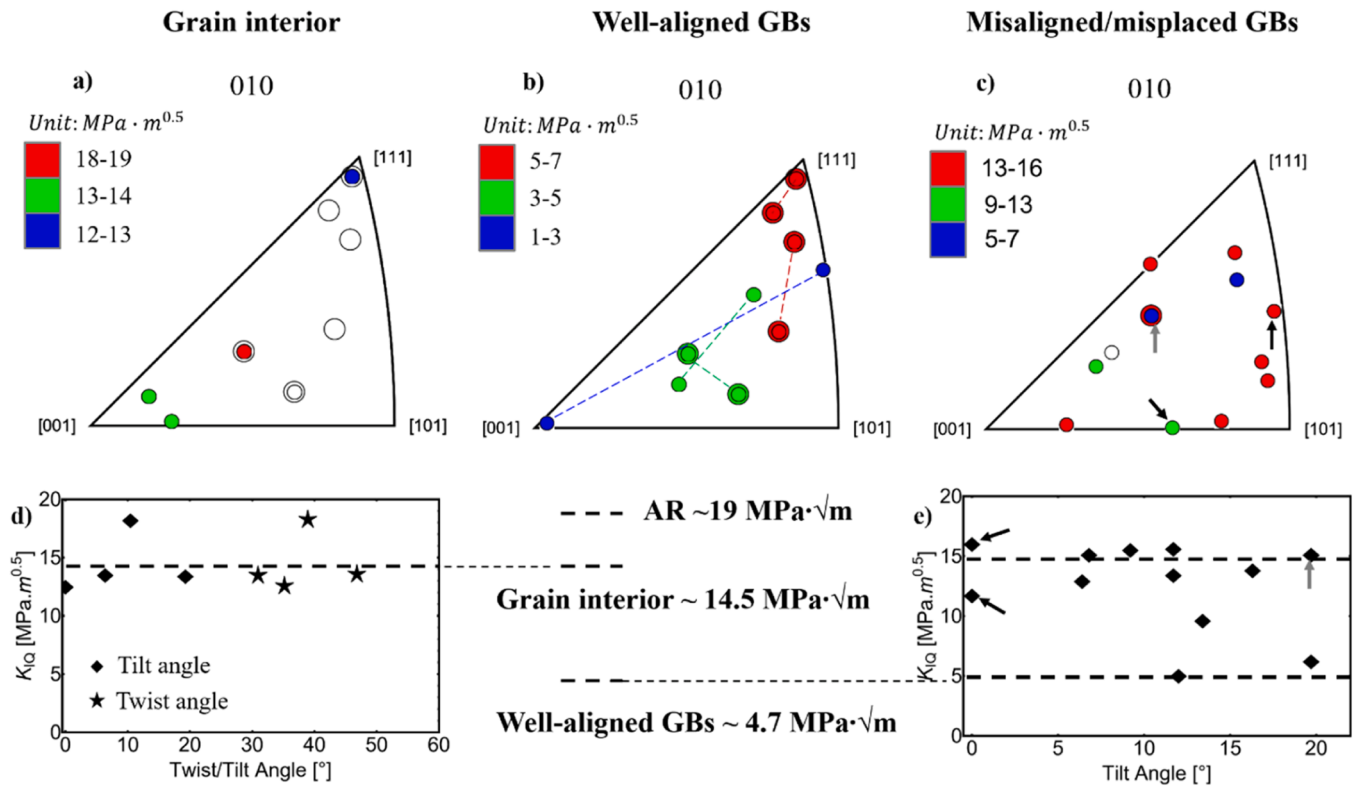


Fig. 7. For RXW (010) IPFs (cantilever side surface) showing the tested cracked plane in the case of (a) grain interior, (b) well-aligned GBs and (c) misaligned/misplaced GBs. The colour scale denotes the fracture toughness magnitude; blue is always the smallest and red the highest while the unfilled points indicate beams without crack evolution. For well-aligned GBs (b), dotted lines link between the crack plane from both grain pairs, while for three GBs 2 cantilevers could be tested on the same GB length, and two points are superimposed. Misplaced notched in (c) are indicated by black arrows, and misplaced & misaligned by a grey arrow. The rest are only misaligned. (d) K_{IQ} of single grains against the tilt and twist angle between notch plane and $\{110\}$ cleavage planes. (e) K_{IQ} of misaligned/misplaced GBs against the tilt angle between notch plane and the GB plane. For the misplaced case, the tilt angle is considered as 0 and plot as indicated by the black arrows, misaligned & misplaced by the grey arrow. A comparison of toughness results is also highlighted in the figure, including for the as-received (AR) sample. The data presented in this figure is tabulated in Table 2. (For interpretation of the references to colour in this figure legend, the reader is referred to the web version of this article.)

was performed on two different GBs to determine whether the GB chemistry may play a role in the embrittlement observed at the random HAGBs. The two GBs studied had misorientation angles of 44.2° and 24.5° as determined from EBSD analysis of the specimen location, allowing for insights into whether misorientation plays a role in GB chemistry. Both APT specimens showed strong phosphorous segregation at the GBs, as highlighted by the 0.7 at.% iso-concentration surfaces for phosphorous (Fig. 8 and Supplementary Information Fig. S5). Concentration analysis of the APT specimens showed a peak concentration of ~ 2.5 at.% phosphorous at the GBs, with negligible phosphorous signal in the tungsten matrix of (0.009 ± 0.002) at.% based on two APT tips in the vicinity of the investigated GBs (Fig. S5). There was no observable dependence of the misorientation angle on the magnitude of the phosphorous signal. This concentration is equivalent to a Gibbsian interfacial excess of 8 P atoms/ nm^2 and 5 P atoms/ nm^2 for GB1 and GB2, respectively, calculated according to Refs [45,46]. For comparison, a $\{100\}$ plane of W contains approx. 15 W atoms/ nm^2 . In addition to phosphorous, a subtle enrichment in iron was observed at the GB with a concentration of 0.1 at.%. It should be noted that no signal elevated against the matrix baseline of oxygen was found at the GBs (1D profile of oxygen concentration across GBs provided in Fig. S6).

3.6. Atomistic simulations

For the used W MEAM potential, the lowest fracture toughness was determined for the $\{110\}\langle -110 \rangle$ cracks ($\{\text{plane}\}\langle \text{crackfront} \rangle$) with $K_{Ic} = 1.7 \text{ MPa}\cdot\sqrt{\text{m}}$, followed by $\{001\}\langle 1-10 \rangle$ with $K_{Ic} = 1.95 \text{ MPa}\cdot\sqrt{\text{m}}$

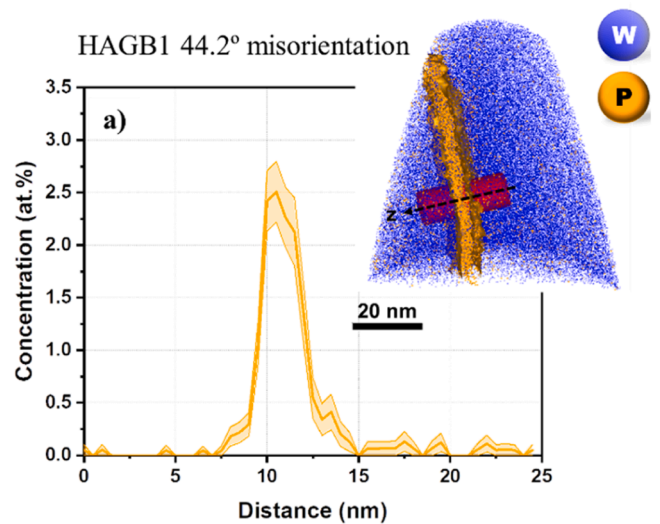


Fig. 8. Grain boundary chemistry investigated by atom probe tomography (APT). One-dimensional concentration profile of phosphorous for HAGB1 with 44.2° misorientation, along the cylinder across the grain boundary shown in the inset three-dimensional APT maps of tungsten and phosphorous. The grain boundary is marked by a 0.7 at.% iso-concentration surface of phosphorous. (For interpretation of the references to colour in this figure legend, the reader is referred to the web version of this article.)

[22]. For the experimentally motivated $(97 \overline{18} \overline{8})[0 4 \overline{9}]$ crack system which is close to a $(1 0 0)[0 1 \overline{1}]$ crack our simulations resulted in $K_{Ic} = 1.96 \text{ MPa}\cdot\sqrt{\text{m}}$, see Table S2 in the Supplementary Information. A deviation of about 11° of the crack plane from the ideal $(1 0 0)$ plane just resulted in about 1% increase in K_{Ic} . The same crack system with 2.5 at. % P led to $K_{Ic} = 1.8 \text{ MPa}\cdot\sqrt{\text{m}}$, a roughly 9% reduction.

The final, relaxed structure of the experimentally-motivated asymmetric high-angle tilt $\Sigma 7 [111] 38.21^\circ (8 -3 -5)/(1 -1 0)$ GB are shown in Fig. S2. The GB structure is rather compact without simple structural units that are often observed in symmetric low Σ GBs. However, the $\Sigma 7$ periodicity is clearly visible, e.g., in the periodic blue atoms on the B-side of the GB in Fig. S2a). The MD/MC simulation to mimic diffusion during the heat treatment led to a clear segregation of P to the GB, with ~ 2.5 at.% concentration of P in the GB. The GB structure is much more disordered and locally wider than for the pure W GB.

The results of the strain-controlled GB fracture are shown in Figs. 9 and 10 as well as in Table S3 in the Supplementary Information. Cracks in pure W showed well-defined critical strains ϵ_{cr} at which the GBs fractured. In contrast, in the P-segregated GB the propagating crack can be locally arrested one or multiple times, requiring strain increases to propagate throughout the sample, see Fig. 10. Therefore, we introduce the critical strain for the initiation of crack propagation, $\epsilon_{cr,ini}$, and the critical strain for final fracture, $\epsilon_{cr,fin}$. The simulations clearly

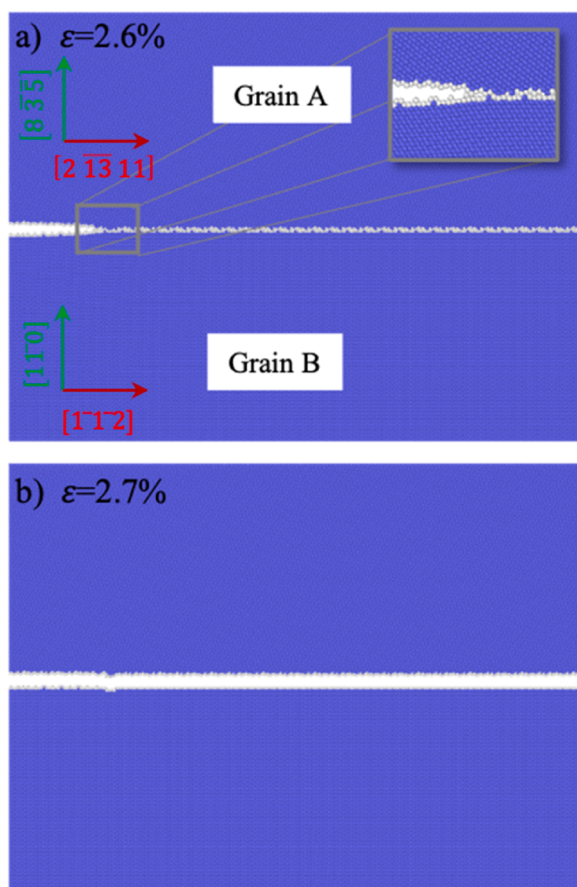


Fig. 9. Simulation setup and critical strain for fracture of the asymmetric high-angle tilt $\Sigma 7 [111] 38.21^\circ (8 -3 -5)/(1 -1 0)$ GB. (a) shows the orientations of grain A and B and a stable crack upon relaxation at a strain of $\epsilon = 2.6\%$. The GB approximates the experimentally tested GB B7, which is shown in Fig. 5. (b) shows that the GB crack has completely cleaved the sample at $\epsilon_{cr,ini} = \epsilon_{cr,fin} = 2.7\%$. Blue atoms correspond to W atoms in a bcc lattice, while white atoms are atoms identified by CNA as belonging to a defect. The inset shows the magnified crack tip configuration. (For interpretation of the references to colour in this figure legend, the reader is referred to the web version of this article.)

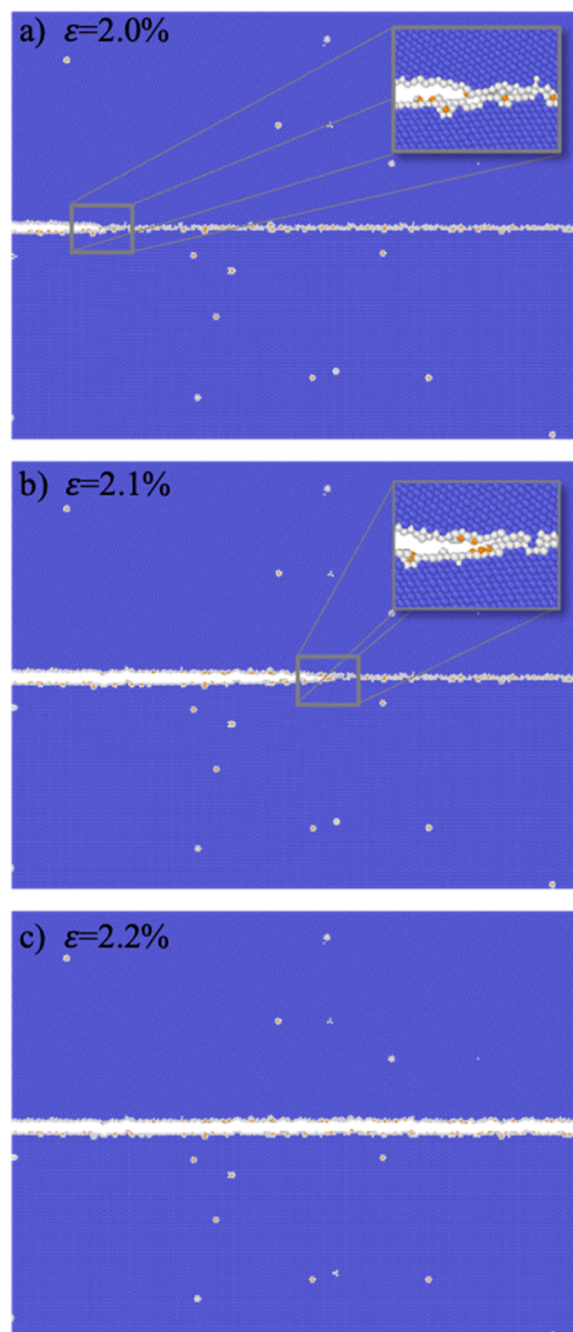


Fig. 10. Fracture of the P-segregated $\Sigma 7$ GB. Orientation and colour code are identical to Fig. 9, with P atoms shown in orange. (a) stable GB crack configuration; (b) relaxed, arrested crack at $\epsilon_{cr,ini} = 2.1\%$; (c) fully cleaved sample at $\epsilon_{cr,fin} = 2.2\%$. (For interpretation of the references to colour in this figure legend, the reader is referred to the web version of this article.)

demonstrate a significant reduction in fracture strain of about 20% by the segregation of P to the GB.

Various fracture mechanisms could be observed for cracks not directly placed on the GB. The different observed mechanisms are exemplarily shown in Fig. 11 and Fig. S7 and provided for all performed simulations in Table S3 in the Supplementary Information:

- Straight propagation of a cleavage crack (Fig. 11(a)) can be observed when the crack is placed far enough from the GB in grain B. There, the plane parallel to the crack plane corresponds to the natural (110)

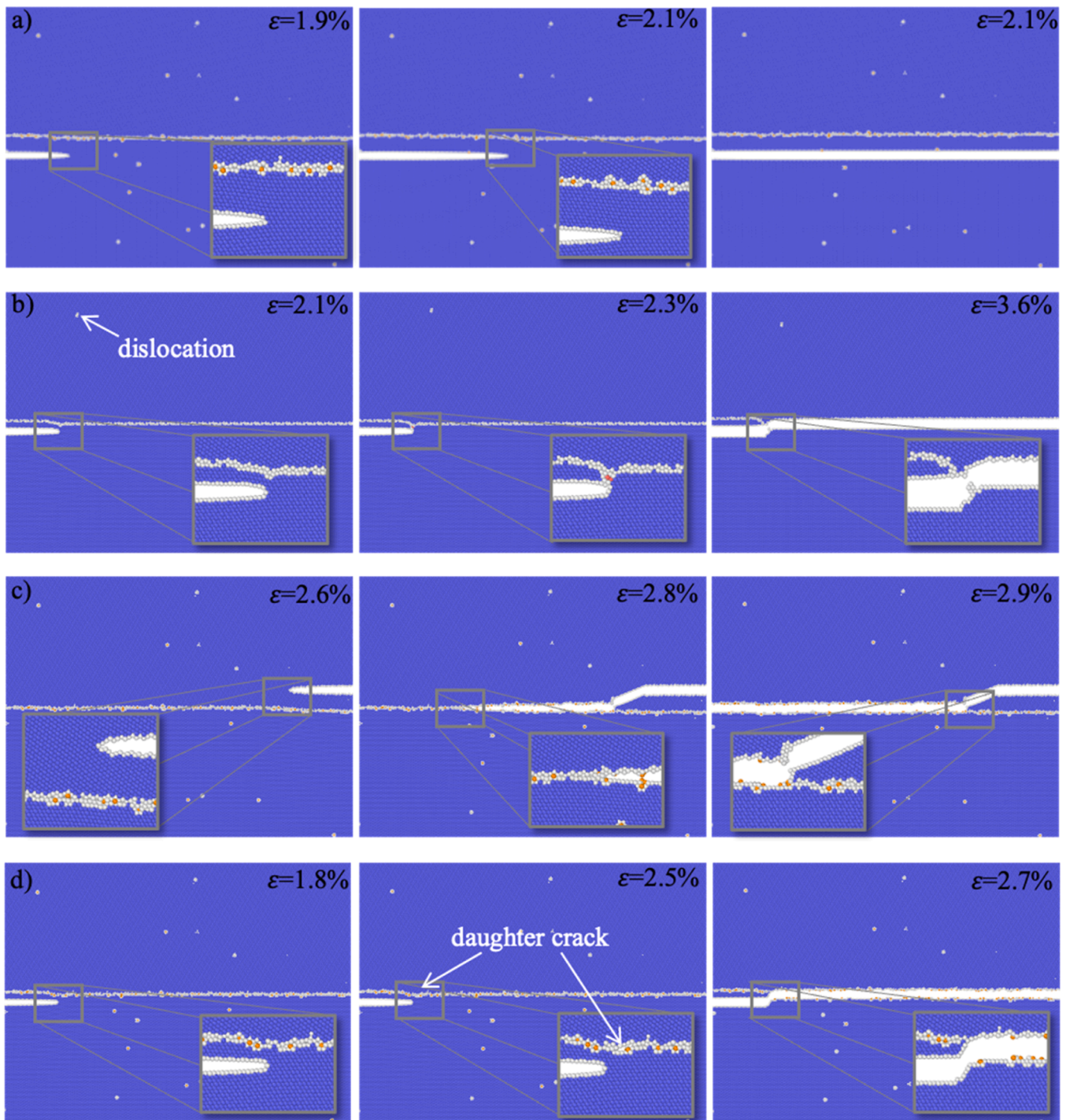


Fig. 11. Different fracture mechanisms for cracks that are not initially placed on the GB. For the colour code and the crystallographic orientations see Figs. 9 and 10. (a) Cleavage along the $(1\bar{1}0)$ plane in grain B in the P-containing case. The same cleavage takes also place in pure W, but is only observed in grain B. (b) Upon initial minimisation a dislocation is emitted from the GB and the GB plastically deforms towards the crack until the crack joins the GB and propagates along the GB. This mechanism takes place only in pure W. Dislocation emission and GB plasticity also occur if the crack is further away and cannot join the GB but propagates within the grain. (c) Deviation of the crack from the initial plane onto a $\{110\}$ plane towards the crack and transgranular fracture. This mechanism takes place with or without P but only in grain A (the crack can also propagate away from the GB). (d) Formation of a daughter crack in the GB, cleavage along the GB and merging with the initial crack. This mechanism has only been observed for P-containing GBs. (For interpretation of the references to colour in this figure legend, the reader is referred to the web version of this article.)

low-energy cleavage plane. This is the case with and without P, however, the amount of GB deformation is larger for the pure GB.

- For cracks parallel to the GB in pure W, dislocation emission from the GB is always observed (Fig. 11(b)), but never when P is present at the GB.

- When the crack is relatively close to the GB, the GB can additionally plastically deform and bow towards the crack tip. This can lead to the crack propagating along the GB (Fig. 11(b)).
- Cracks in grain A can – with or without P at the GB – deviate onto $\{110\}$ planes and meet the GB and then propagate in an intergranular

way, or move away from the crack, depending on the initial direction of the crack (Fig. 11(c)).

- Finally, cracks can lead to the nucleation of a daughter crack on the GB, which propagates and joins the initial crack (Fig. 11(d)). This mechanism has only been observed for P-containing GBs.

Interestingly, whether the crack is situated directly on the GB or placed parallel to it at different distances, *the presence of P always leads to a reduction of the critical fracture strain compared to the pure system, independent of the fracture mechanism*. Based on the observation that no dislocations are emitted from the grain boundary when it is segregated and that the GB deforms less when P is present (compare Fig. 11(b) and (d)), it appears plausible that P at the GB reduces GB plasticity. Less plastic dissipation in turn automatically leads to a lower fracture toughness. This aspect might be important to consider in addition to the loss of cohesive strength due to P segregation, see e.g. Ref. [20].

4. Discussion

4.1. Fracture toughness of RXW

The room temperature toughness values obtained for the single crystalline cantilevers of $\sim 14.5 \text{ MPa}\cdot\sqrt{\text{m}}$ are significantly higher than those reported for microcantilever toughness of tungsten single crystals with the notch aligned along the $\{100\}\langle 010 \rangle$ cleavage plane of $\sim 6 \text{ MPa}\cdot\sqrt{\text{m}}$ [28] and $8\text{--}12 \text{ MPa}\cdot\sqrt{\text{m}}$ [29] where ligament length ($W-a_0$) and loading rate were found to influence the toughness magnitude. For context, at the macroscale and at room temperature, the toughness of cleavage systems $\{100\}\langle 010 \rangle$, $\{100\}\langle 011 \rangle$ and $\{110\}\langle 001 \rangle$ have been evaluated as 8.7 ± 2.5 , 6.2 ± 1.7 and $20.2 \pm 5.5 \text{ MPa}\cdot\sqrt{\text{m}}$, respectively [47]. Our single-crystal results are more in line with results obtained by Wurster *et al.* for single-crystal tungsten using both *J*-integral and CTOD approaches. They found that if the notch plane is rotated away 25° from the $\{100\}$ plane along an axis orthogonal to the notch front direction (i. e. ‘twisted’), the fracture toughness of W can increase by $\sim 20\%$ [30]. The single crystal simulations for the misoriented crack system $(97 \overline{18} 8)[0 \ 4 \ \overline{9}]$ showed, however, only a moderate increase in fracture toughness. This crack system was, however, mostly mode-mixed (with tilt and twist angles of 11° and 19° , respectively) to the $(110)[\overline{1}10]$ natural crack system. Currently there is no detailed, systematic study of the influence of the ‘tilt’ angle through which the crack plane is misaligned with respect to a natural cleavage plane. In any case, the fracture toughness is no longer defined by only one value, as the loading conditions are multimodal.

In the careful work of Ref. [28], microcantilevers have only been reported to fail in a brittle manner to a maximum $W-a_0$ of $1.8 \mu\text{m}$ when aligned to the $\{100\}\langle 010 \rangle$ cleavage system. A toughness of $\sim 6 \text{ MPa}\cdot\sqrt{\text{m}}$ was additionally determined for ultrafine-grained tungsten (790 nm) containing a large number of grain boundaries, rationalised by a high likelihood of any number of grains to present a favourable orientation for crack growth (similar onset for crack growth in single crystals), while brittle failure was avoided through interaction of the cracks with grain boundaries (also reported at bulk-scales [27]). This observation is in contrast to the results for RXW of the present study, where all cantilevers with the notch well aligned to the grain boundary failed in a brittle manner ($1 < W-a_0 < 4$), with a fracture toughness ($4.7 \pm 0.4 \text{ MPa}\cdot\sqrt{\text{m}}$ not related to ligament length; significantly lower than that reported for cleavage fracture at both bulk and microscales. Indeed, the misaligned notch/GB plane experiments in Fig. 6 highlight the brittle nature of GBs, irrespective of mode mixity (when comparing purely misaligned to *misplaced* notches, as the latter do not experience mixed mode loading).

The GB toughness of RXW is found here to be insensitive to the crystal orientation of each grain pair (Fig. 7(a)–(c)), angular offset to the closest cleavage plane (Fig. 7(d), (e)), or the magnitude of the GB misorientation angle (Fig. S4). Moreover, GBs tested in the as-received

condition showed toughness results comparable to the single-crystalline beams. Indeed, the only clear factor seemingly affecting toughness at the GB is the grain boundary chemistry, where phosphorous was recently calculated to weaken the cohesion in tungsten GBs from *ab initio* DFT simulations [25]. In that work, the difference in the segregation energy of phosphorous atoms on a GB and a free surface was calculated, and a positive strength of embrittlement was determined. Similarly, our atomistic simulation using a more complex GB clearly demonstrates, *i*) that P segregates to the GB, forming complex, irregular segregation patterns (in contrast to the highly-idealised situation in DFT calculations); and that *ii*) the fracture toughness of P-containing GBs is significantly reduced.

Investigations on the role of phosphorous using secondary ion mass spectroscopy have previously concluded that an average content of 20–40 ppm (0.002–0.004 at.%) phosphorous does not influence the fracture behaviour of tungsten, and only higher concentrations can increase the embrittlement [48]. The experimental fracture toughness of isolated GBs in tungsten without the presence of secondary elemental species has not yet been studied. Based on the thermodynamic argument by Griffith, individual GBs should always have lower fracture toughness than cracks within the grains when those run along planes that are parallel to the GB plane. In this case, the energy needed to create the GB is gained back. This is, however not the case if lower energy fracture planes are available. These can lead to preferential intragranular fracture. Some recent observations have pointed towards the importance of also considering kinetic effects such as bond trapping when comparing intergranular with intragranular fracture [49]. In general, however, observations on single GBs cannot be transferred to polycrystals as *i*) the whole spectrum of GB fracture toughness would have to be considered, and *ii*) the additional increase of crack area through the corrugated crack path along GBs would need to be considered [15].

4.2. Origins of GB phosphorous localisation in RXW

A practical consideration is to determine from where the excess phosphorous originates, and whether phosphorous is also present in the as-received material. To determine this, a single APT tip was successfully extracted at a random HAGB for the as-received material and analysed (Fig. S8). Interestingly, at the HAGBs of the as-received material a statistically significant concentration of phosphorous was also observed at the GB with a maximum of ~ 0.07 at.% phosphorous (Gibbsian interfacial excess of $0.2 \text{ atoms}/\text{nm}^2$). This is significantly lower than the 2.5 at.% phosphorous measured at the GB of the RXW material, but clearly indicates that phosphorous is indeed present in the as-received material and segregated to GBs. Further, two APT tips of as-received material containing no GBs were also analysed. Negligible phosphorous was detected in the matrix, as suggested by the APT mass-to-charge spectrum in Fig. S9. Thus, it is worth noting that the residual phosphorous signal in the matrix regions of ($\sim 0.009 \pm 0.002$) at.% observed in the RXW sample (Fig. 8) is likely a detection artefact from the background signal in the mass spectrum. In addition to phosphorous, a small concentration of iron was again observed (~ 0.05 at.%), which is consistent with the iron concentration at GBs measured in the RXW sample.

The increased phosphorous concentration at the GB for RXW can be rationalised considering the significant grain growth during recrystallisation (and consequent reduction in GB area). Compared with the grains of diameter (1.8 ± 1.0) μm (using the line-intercept method on the SEM image of Fig. S8b) in the as-received sample, the grain size of the RXW sample is increased by approximately 11 times with a value of (19 ± 7) μm (from EBSD image Fig. 2(b)). Assuming spherical grains and calculating the GB area ratio for both as-received and RXW, a value of 7.8 at.% P (or $22 \text{ atoms}/\text{nm}^2$) is estimated for RXW based on the 0.07 at.% P measured for as-received GBs (Fig. S8a). This estimate is $\sim 3\times$ larger than what was measured for RXW GBs (Fig. 8), however is an upper bound, assuming that during recrystallisation phosphorous only goes to GBs, and not to surfaces, dislocations or triple junctions. As such, the

enhancement of phosphorous at random HAGBs results from high driving forces for the reduction of the GB energy (already occurring during the initial processing of the material) as formalised in terms of Gibbs adsorption isotherm, and a large decrease in GB area due to grain growth. This correlates well to the microcantilever testing of the as-received material, where a fracture toughness comparable to that of the single crystal RXW sample was determined (with no brittle intergranular fracture observed) when placing a GB under the notch tip (Fig. 2). This serves as a direct experimental evidence that the increased P content induced by recrystallisation and grain growth promotes GB embrittlement, and is further strengthened by the atomistic simulations results of Figs. 9 and 10.

This analysis aligns strongly with investigations in the 1970s, where Auger spectroscopy analyses showed the segregation of phosphorous to GBs in RXW to be the main cause of the brittle behaviour of tungsten [50]. It was also found that the amount of phosphorous segregation was dependent upon the grain size – the larger the grain size, the greater the concentration of phosphorous at the GB and the higher the embrittlement effect [50]. The recent report of Gludovatz *et al.*, however, contrasts to our observations and the result in Ref. [50]. Gludovatz *et al.* found no significant embrittlement effect of impurities in polycrystalline tungsten, while microstructure (grain morphology and dislocation density) was proposed to be more critical [23]. There, the reduced portion of intergranular brittle fracture in samples with larger grains was attributed to the bimodal distribution of grain size, which requires more deviation by cleavage to follow the macroscopic crack path. While for polycrystalline tungsten, the grain shape, grain size and other microstructural features might play a more dominant role in intergranular fracture than the impurity at GBs, such microstructure effects are minimised for bicrystalline microcantilever testing, which captures the precise influence of phosphorous segregation. Furthermore, based on the as-received sample results (Fig. 2) with smaller grain sizes and significantly less GB segregation, no catastrophic intergranular failure is observed, suggesting that there is a critical impurity limit for fracture to occur along the GBs. When broadly discussing an impurity limit, however, it is more important to consider the grain size and how the impurities are locally distributed on the GBs rather than their nominal content. As demonstrated in the present study, an increase in grain size (resulting in a decrease in GB area) can enhance the localised concentration of phosphorous at GBs, leading to a significant embrittling effect, while the fracture toughness is not related to the geometrical (or macroscopic) degrees of freedom of the HAGBs.

5. Conclusions

In this study, clear inferences were made between the local chemical composition and toughness at grain boundaries in tungsten using a combination of site-specific microcantilever fracture toughness testing, APT, and targeted atomistic simulations. Segregation of phosphorous at GBs was observed in both as-received and recrystallised samples, which could be driven by the requirement for the reduction of the GB energy (Gibbs adsorption isotherm). The atomistic simulations also showed clearly the segregation of phosphorous to the GB. While the as-received tungsten showed a phosphorous concentration of 0.07 at.% at grain boundaries, the recrystallised sample revealed a much higher phosphorous concentration of ~2.5 at.% at two random HAGBs with different misorientation angles. This more pronounced segregation of phosphorous at grain boundaries was attributed to the grain growth during recrystallisation at 1600 °C for 1 h, which reduced the total grain boundary area available for segregation. Targeted microcantilever tests at the grain boundary suggested a significant effect of phosphorous segregation on mechanical response; the toughness sharply dropped to $4.7 \pm 0.4 \text{ MPa}\cdot\sqrt{\text{m}}$ at the grain boundary from $14.5 \pm 1.3 \text{ MPa}\cdot\sqrt{\text{m}}$ for randomly aligned notches in single crystals (i.e., misaligned from the cleavage plane) and $\sim 19 \text{ MPa}\cdot\sqrt{\text{m}}$ for GBs on the as-received material. It was found that the toughness results were not related to any

discernible crystallographic descriptors of the GBs but were solely affected by the impurity segregation of phosphorous. These results were supported by atomistic simulations, which clearly demonstrated a reduction in fracture strain of ~20% by the segregation of P to an asymmetric $\Sigma 7$ GB that was modelled after the experiments. These showed that even misplaced cracks parallel to the GB were affected by the presence of phosphorous at the GB. P-segregation led to reduced GB plasticity and the formation of daughter cracks on the GB, both mechanisms that decrease the fracture toughness. In contrast, energy dissipation by dislocation emission from GBs further increases the fracture toughness of pure tungsten. The correlative, site-specific micro-mechanics and APT combined with experimentally-informed atomistic simulations thus proved a powerful approach to uncover relationships between defect chemistry and the mechanical response of materials.

Declaration of Competing Interests

The authors declare that they have no known competing financial interests or personal relationships that could have appeared to influence the work reported in this paper.

Acknowledgements

Leon Christiansen from MPIE is thanked for his support with the fabrication and testing. The funding and support by the European Research Council (ERC) under the EU's Horizon 2020 Research and Innovation Program is gratefully acknowledged by GD (ERC Advanced Grant, GB-Correlate, Grant no. 787446) and AG, PP, EB (ERC Consolidator Grant, microKIC, Grant no. 725483).

Supplementary materials

Supplementary material associated with this article can be found, in the online version, at doi:10.1016/j.actamat.2023.119256.

References

- [1] F. Romanelli, Overview of the JET results with the ITER-like wall, *Nucl. Fusion* 53 (10) (2013), 104002.
- [2] A. Kallenbach, Overview of ASDEX upgrade results, *Nucl. Fusion* 57 (10) (2017), 102015.
- [3] J. Bucalossi, et al., Operating a full tungsten actively cooled tokamak: overview of WEST first phase of operation, *Nucl. Fusion* 62 (4) (2022), 042007.
- [4] R.A. Pitts, et al., Physics basis for the first ITER tungsten divertor, *Nucl. Mater. Energy* 20 (2019), 100696.
- [5] V. Philipps, Tungsten as material for plasma-facing components in fusion devices, *J. Nucl. Mater.* 415 (1, Supplement) (2011) S2–S9.
- [6] G. Pintsuk, A. Hasegawa, 6.02—Tungsten as a plasma-facing material, in: R.J. M. Konings, R.E. Stoller (Eds.), *Comprehensive Nuclear Materials*, second ed., Elsevier: Oxford, 2020, pp. 19–53.
- [7] S. Brezinsek, et al., Fuel retention studies with the ITER-like wall in JET, *Nucl. Fusion* 53 (8) (2013), 083023.
- [8] C. Yin, et al., Ductile to brittle transition in ITER specification tungsten assessed by combined fracture toughness and bending tests analysis, *Mater. Sci. Eng.* 750 (2019) 20–30.
- [9] V. Shah, et al., Brittle-ductile transition temperature of recrystallized tungsten following exposure to fusion relevant cyclic high heat load, *J. Nucl. Mater.* 541 (2020), 152416.
- [10] S. Bonk, et al., Cold rolled tungsten (W) plates and foils: evolution of the tensile properties and their indication towards deformation mechanisms, *Int. J. Refract. Metals Hard Mater.* 70 (2018) 124–133.
- [11] A. Durif, et al., Impact of tungsten recrystallization on ITER-like components for lifetime estimation, *Fusion Eng. Des.* 138 (2019) 247–253.
- [12] M. Richou, et al., Recrystallization at high temperature of two tungsten materials complying with the ITER specifications, *J. Nucl. Mater.* 542 (2020), 152418.
- [13] M. Minissale, et al., Grain growth and damages induced by transient heat loads on W, *Phys. Scr.* 96 (12) (2021), 124032.
- [14] P. Lejček, M. Sob, V. Paidar, Interfacial segregation and grain boundary embrittlement: an overview and critical assessment of experimental data and calculated results, *Prog. Mater. Sci.* 87 (2017) 83–139.
- [15] A.P. Sutton, R.W. Balluffi, *Interfaces in Crystalline Materials*, Oxford University Press, 1995.
- [16] S. Hofmann, H. Hofmann, Influence of grain boundary segregation on mechanical properties of activated sintered tungsten, *J. Phys. Colloq.* 46 (C4) (1985), C4-633–C4-640.

- [17] L. Zhi-Wu, et al., Segregation of alloying atoms at a tilt symmetric grain boundary in tungsten and their strengthening and embrittling effects, *Chin. Phys. B* 23 (10) (2014), 106107.
- [18] P. Zhiliang, L.J. Kecskes, Q. Wei, The nature behind the preferentially embrittling effect of impurities on the ductility of tungsten, *Comput. Mater. Sci.* 93 (2014) 104–111.
- [19] P.A.T. Olsson, J. Blomqvist, Intergranular fracture of tungsten containing phosphorus impurities: a first principles investigation, *Comput. Mater. Sci.* 139 (2017) 368–378.
- [20] P.A.T. Olsson, P. Hiremath, S. Melin, Atomistic investigation of the impact of phosphorus impurities on the tungsten grain boundary decohesion, *Comput. Mater. Sci.* 219 (2023), 112017.
- [21] J.J. Möller, E. Bitzek, Fracture toughness and bond trapping of grain boundary cracks, *Acta Mater.* 73 (2014) 1–11.
- [22] P. Hiremath, S. Melin, E. Bitzek, P.A.T. Olsson, Effects of interatomic potential on fracture behaviour in single-and bicrystalline tungsten, *Comput. Mater. Sci.* 207 (2022), 111283.
- [23] B. Gludovatz, et al., Influence of impurities on the fracture behaviour of tungsten, *Philos. Mag.* 91 (22) (2011) 3006–3020.
- [24] L. Tran Huu, et al., Brittle fracture of polycrystalline tungsten, *J. Mater. Sci.* 20 (1) (1985) 199–206.
- [25] D. Scheiber, et al., Ab initio search for cohesion-enhancing impurity elements at grain boundaries in molybdenum and tungsten, *Model. Simul. Mater. Sci. Eng.* 24 (8) (2016), 085009.
- [26] Wagih, M., Schuh, C.A., *Can symmetric tilt grain boundaries represent polycrystals?* arXiv, 2023. DOI: 10.48550/arXiv.2306.17336.
- [27] R.W. Margevicius, J. Riedle, P. Gumbsch, Fracture toughness of polycrystalline tungsten under mode I and mixed mode I/II loading, *Mater. Sci. Eng.* 270 (2) (1999) 197–209.
- [28] J. Ast, M. Göken, K. Durst, Size-dependent fracture toughness of tungsten, *Acta Mater.* 138 (2017) 198–211.
- [29] J. Ast, et al., The brittle-ductile transition of tungsten single crystals at the micro-scale, *Mater. Des.* 152 (2018) 168–180.
- [30] S. Wurster, C. Motz, R. Pippin, Characterization of the fracture toughness of micro-sized tungsten single crystal notched specimens, *Philos. Mag.* 92 (14) (2012) 1803–1825.
- [31] M. Wurmshuber, et al., Tuning mechanical properties of ultrafine-grained tungsten by manipulating grain boundary chemistry, *Acta Mater* 232 (2022), 117939.
- [32] S. Brinckmann, et al., On the influence of microcantilever pre-crack geometries on the apparent fracture toughness of brittle materials, *Acta Mater.* 136 (2017) 281–287.
- [33] ASTM Standard E399, *Standard Test Method for Linear-Elastic Plane-Strain Fracture Toughness K_{Ic} of Metallic Materials*. 2018.
- [34] K. Matoy, et al., A comparative micro-cantilever study of the mechanical behavior of silicon based passivation films, *Thin Solid Films* 518 (1) (2009) 247–256.
- [35] R. Pippin, S. Wurster, D. Kiener, Fracture mechanics of micro samples: fundamental considerations, *Mater. Des.* 159 (2018) 252–267.
- [36] ASTM Standard E1820, *Standard Test Method for Measurement of Fracture Toughness*. 2018.
- [37] S. Plimpton, P. Crozier, A. Thompson, LAMMPS-large-scale atomic/molecular massively parallel simulator, *Sandia Natl. Lab.* 18 (2007) 43.
- [38] R. Valerie, *The Measurement of Grain Boundary Geometry*, CRC Press, 2017.
- [39] M.A. Tschopp, S.P. Coleman, D.L. McDowell, Symmetric and asymmetric tilt grain boundary structure and energy in Cu and Al (and transferability to other fcc metals), *Integr. Mater. Manuf. Innov.* 4 (2015) 176–189.
- [40] Y. Sheng, et al., Atomistic simulations of dislocation mobility in refractory high-entropy alloys and the effect of chemical short-range order, *Nat. Commun.* 12 (1) (2021) 4873.
- [41] J. Guérolé, et al., Assessment and optimization of the fast inertial relaxation engine (fire) for energy minimization in atomistic simulations and its implementation in lammps, *Comput. Mater. Sci.* 175 (2020), 109584.
- [42] J.J. Möller, *Atomistic Simulations of Crack Front Curvature Effects and Crack-Microstructure Interactions*, FAU University Press, 2017.
- [43] A. Stukowski, Structure identification methods for atomistic simulations of crystalline materials, *Model. Simul. Mater. Sci. Eng.* 20 (4) (2012), 045021.
- [44] A. Stukowski, Visualization and analysis of atomistic simulation data with OVITO—the open visualization tool, *Model. Simul. Mater. Sci. Eng.* 18 (1) (2009), 015012.
- [45] M.J.R. Sandim, et al., Grain boundary segregation in a bronze-route Nb₃Sn superconducting wire studied by atom probe tomography, *Supercond. Sci. Technol.* 26 (5) (2013), 055008.
- [46] B.M. Jenkins, et al., Reflections on the analysis of interfaces and grain boundaries by atom probe tomography, *Microsc. Microanal.* 26 (2) (2020) 247–257.
- [47] J. Riedle, P. Gumbsch, H.F. Fischmeister, Cleavage anisotropy in tungsten single crystals, *Phys. Rev. Lett.* 76 (19) (1996) 3594–3597.
- [48] H. Danninger, F. Knoll, B. Lux, Phosphorus embrittlement of tungsten heavy alloys, *Int. J. Refract. Hard Met.* 4 (2) (1985) 92–96.
- [49] J.J. Möller, E. Bitzek, Fracture toughness and bond trapping of grain boundary cracks, *Acta Mater.* 73 (2014) 1–11.
- [50] A. Joshi, D. Stein, Intergranular brittleness studies in tungsten using Auger spectroscopy, *Metall. Trans.* 1 (9) (1970) 2543–2546.